



LAWRENCE
LIVERMORE
NATIONAL
LABORATORY

Ramp Compression of Diamond at 5 TPa

R. F. Smith, J. H. Eggert, R. Jeanloz, T. S. Duffy, D. G.
Braun, J. R. Patterson, R. E. Rudd, J. Biener, A. E.
Lazicki, A. V. Hamza, J. Wang, T. Braun, L. X.
Benedict, P. M. Celliers, G. W. Collins

March 13, 2014

Nature

Disclaimer

This document was prepared as an account of work sponsored by an agency of the United States government. Neither the United States government nor Lawrence Livermore National Security, LLC, nor any of their employees makes any warranty, expressed or implied, or assumes any legal liability or responsibility for the accuracy, completeness, or usefulness of any information, apparatus, product, or process disclosed, or represents that its use would not infringe privately owned rights. Reference herein to any specific commercial product, process, or service by trade name, trademark, manufacturer, or otherwise does not necessarily constitute or imply its endorsement, recommendation, or favoring by the United States government or Lawrence Livermore National Security, LLC. The views and opinions of authors expressed herein do not necessarily state or reflect those of the United States government or Lawrence Livermore National Security, LLC, and shall not be used for advertising or product endorsement purposes.

Ramp Compression of Diamond to 5 TPa

R.F. Smith¹, J.H. Eggert¹, R. Jeanloz³, T.S. Duffy², D.G. Braun¹, J.R. Patterson¹,
R.E. Rudd¹, J. Biener¹, A.E. Lazicki¹, A.V. Hamza¹, J. Wang², T. Braun¹, L.X. Benedict¹,
P.M. Celliers¹, G.W. Collins¹

¹*Lawrence Livermore National Laboratory, P.O. Box 808, Livermore, CA 94550, USA*

²*Department of Geosciences, Princeton University, Princeton, NJ 08544, USA*

³*Department of Earth and Planetary Science, Department of Astronomy and Miller
Institute for Basic Research in Science, University of California, Berkeley, CA 94720,
USA*

The recent discovery of hundreds of planets outside our Solar System^{1,2} together with the significant push to achieve inertially confined fusion in the laboratory³ has prompted a renewed interest in how dense matter behaves at millions to billions of atmospheres pressure. The theoretical description of such electron-degenerate matter has matured since the early quantum statistical model of Thomas-Fermi⁴⁻¹⁰, and now suggests that new complexities can emerge at pressures where core electrons - not just valence electrons - influence the structure and bonding of matter.¹¹ Recent developments in shock-free dynamic (ramp) compression now allow the first laboratory access to this dense matter regime. We describe new ramp-compression measurements for diamond, achieving 3.7-fold compression at a peak pressure of 5 terapascal (5 TPa = 50 million atmospheres). These equation-of-state data are compared to and provide the first experimental benchmark for first-principles density-functional calculations (DFT)¹² and theories long used to describe matter present in the interiors of giant planets, in stars, and in inertial-confinement fusion experiments. Our data also furnish new constraints on mass-radius relationships for carbon-rich planets.

Mass-radius data for extra-solar planets combined with equation-of-state (EOS) models for constituent materials reveal that matter at several TPa pressure is quite common throughout the universe.^{1,2,13} At several TPa, matter is approaching an atomic scale pressure (e.g. quantum-mechanical “pressure” that counteracts the electrons’ Coulomb attraction in a Bohr atom), where material structure and chemistry, and even the properties of atoms themselves are expected to change¹¹. Recent DFT calculations predict that in several materials the localization of electrons at TPa conditions produces an electride-like phase with structural and electronic complexity unexpected from quantum statistical models (e.g. Thomas-Fermi).¹²

Experimental access to multi-TPa conditions is now possible with dynamic-ramped-compression. Dynamic compression is necessary to achieve atomic-scale pressures, conditions far beyond those accessible in static experiments¹⁴. Ramp compression produces less dissipative-heating, thus enabling higher compression and lower temperature, as compared to shock compression¹⁵. Ramp compression is however unstable relative to a shock because sound velocities typically increase with pressure, so precise control of the applied pressure-loading history is required to achieve high pressures without shock formation.

The National Ignition Facility, a 2-MJ (megajoule) laser designed to create thermonuclear fusion in the laboratory³, offers the energy and control necessary to ramp compress matter to several TPa. This report summarizes ramp-loading measurements on carbon to 5 TPa, with stress, density and sound speed determined for the entire compression path. These new data are at unprecedented conditions, providing the first experimental constraints on the carbon equation-of-state at pressures more than thirty times previous static-compression measurements, and where state-of-the-art DFT coincides with modern versions of the quantum-statistical Thomas-Fermi model, originally developed early in the last century to describe matter at extreme compressions.

In these experiments, 176 laser beams deliver a total of 2.2 TW peak power, with accuracy better than 1 percent in power and 0.02 ns in time, over 20-ns duration. The light hitting a target (indirectly) creates an ablatively driven pressure wave in the sample (Fig. 1), and – as pressure scales as the 7/8 power of the laser intensity¹⁶ – the pressure is controlled to better than 1 percent. Samples consist of nanocrystalline diamond, shaped with steps so that the pressure-wave transit across four different thicknesses is recorded for each experiment. Response of the sample is characterized by velocity interferometry (VISAR), which records the velocity of the sample’s free (back) surface as it is engulfed by the pressure wave (Fig. 1). Iterative Lagrangian analysis is used to translate these velocity data into a stress-density relation that quantifies the loading path (Fig. 2)¹⁷. These data are absolute — not referenced against a standard — which is important for quantifying the EOS and benchmarking condensed-matter theories in the TPa regime.

In detail, we initiate loading with a ~ 0.1 TPa shock wave, prior to the onset of the main ramp-compression (Fig. 1). Such pre-ramp loading of diamond produces a more fluid-like (strength-free) state¹⁸, which is important for reducing the dissipative heating that can limit compression. Longitudinal stress (P_x) – not pressure – is shown in Fig. 2, as our one-dimensional loading method creates a uniaxial strain that relaxes toward an isotropic state.

A typical record (Fig. 1) shows a free-surface velocity profile, $u_{fs}(t)$, characterized by an initial shock to 4.1 km/s, followed by a fast rise and plateau at 7.2 km/s, and subsequent ramp compression to 46.6 km/s (3.7 TPa). Our analysis yields the Lagrangian sound speed (C_L) and P_x as functions of density (ρ) from the measured $u_{fs}(t)$ (Fig. 2).¹⁷ In all, three experiments yielded $C_L(\rho)$ and $P_x(\rho)$ to peak stresses of 2.7, 3.7 and 5 TPa, respectively. C_L decreases abruptly at $u_{fs} = 4.1$ km/s, corresponding to $P_{x,limit} = 0.11$ TPa that is interpreted as the dynamic strength (elastic limit) of diamond. This also shows up as the slight deviation in the stress-density relation near 0.11 TPa (Fig. 2, inset). Hydrodynamic simulations indicate that the rapid rise and plateau at 7.2 km/s corresponds to a reverberating compression wave within the intermediate Au layer (Fig. 1, inset).

These new data are compared to several carbon EOS models into the multi-TPa regime (Fig. 2, Extended Data Fig. 1, Extended Data Table 1, and Methods). A cold curve derived from first-principles density functional theory (DFT)¹², is in good agreement with a Mie-Grüneisen reduction and extrapolation of shock-Hugoniot data collected to 2 TPa. Also shown are the cold curve formulations from Vinet¹⁹ and Birch-Murnaghan²⁰ each fit to existing diamond anvil cell data.^{21,22} (Even at these extreme

pressures, the difference between the room-temperature isentrope and isotherm as well as the cold curve (0 K) are indistinguishable on this scale: for consistency, below we refer to the cold curve.) For reference, the Hugoniot calculated from both DFT (solid red) and a Mie-Grüneisen model (solid orange) are shown in Fig. 2b. The DFT Hugoniot predicts carbon to be liquid and significantly less compressible than the DFT cold curve for stresses above ~ 1 TPa. Differences between the cold curves (grey band) and Hugoniot (orange band) in Fig. 2b, illustrate the uncertainties in using prior data for extrapolating the carbon EOS into the TPa regime.

The cold curve calculated by DFT shows a sequence of phase transformations: diamond \rightarrow BC8 (~ 0.99 TPa), BC8 \rightarrow simple cubic (~ 2.7 TPa),¹² which are apparent in stress-density by corresponding stress plateaus to increased densities (Fig. 2b). No such stress plateaus are apparent in our new data. While phase transformation kinetics can smooth such features²³, determining whether or not these phase transformations occur will require further work.²⁴ Metadynamics calculations for carbon do indicate that the diamond \rightarrow BC8 transition kinetics may be quite slow.²⁵

Static-compression and elasticity measurements^{21,22} up to their highest pressures (0.15 TPa), are indistinguishable from the DFT cold curve and standard EOS model fits to the data (Vinet and Birch-Murnaghan). However when extrapolated to 5 TPa these models differ by $\sim 20\%$ in density (Fig. 2 and Fig. 3, inset). Our new data lie in between these cold curve calculations.

Also consistent with the DFT cold curve are the gradient- (TFD-W) and gradient and correlation- (TFD-Wc) corrected Thomas-Fermi-Dirac EOS's between about 2 and 5 TPa (Fig. 2).⁹ This agreement is notable, because the statistical-atom model considers neither crystal structure nor orbital information whereas DFT includes both. This agreement may be partly fortuitous because carbon might not yet be in its densest crystal structure at these pressures, and the deviation of statistical-atom theories is toward predicting densities that are systematically too low.

Our ramp data achieve higher density than the shock Hugoniot, consistent with temperatures being lower for ramp compression versus shock compression.^{15,26} Moreover, these new data are somewhat less compressible than cold-isothermal compression calculations with DFT over most of the pressure range studied, and modern TFD formulations (TFD-W and TFD-Wc). Both strength and heating can stiffen the stress-density relation with respect to the cold curve so these data should be considered an upper bound for such comparison, and further study is warranted to better understand differences between theory and experiment.

The experimental techniques developed here provide a new capability to experimentally reproduce pressure-temperature conditions deep in planetary interiors. Carbon is the fourth most abundant element in the cosmos and plays a potentially important role in many types of planets, both within and outside the Solar System. One proposed group of super-Earth exoplanets (1-10 Earth masses in size) are those enriched in carbon, and the planet, 55 Cancri e has been proposed as a possible carbon planet²⁷. Figure 3 shows mass-radius relationships for selected known super-Earths together with various hypothetical uniform-composition planets, including a pure carbon planet based on our ramp-compression equation of state. Using the new data, we find the central pressure for a 10 Earth-mass pure carbon planet to be ~ 0.8 TPa. This new capability to reach multi-TPa pressures also enables experimental access to

Jupiter's core pressures²⁸ where extrapolations of earlier shock and static data become unreliable (Fig. 3, inset).

Our results also have relevance for large pulsar planets, such as the companion of millisecond pulsar PSR J1719-1438²⁹. This object has a minimum mass somewhat larger than Jupiter ($1.15 \times 10^{-3} M_{\text{Sun}}$ or 383 Earth masses), and a 2.2 hour orbital period. A carbon-rich composition was suggested based on TFD-Wc results for carbon^{9,29}. The reliability of this form of TFD theory as shown by our experiments supports this interpretation. An extrapolation of our EOS is consistent with TFD-Wc in suggesting an object of this mass made of pure carbon would have a radius of ~ 4.5 Earth radii and a central pressure of ~ 148 TPa. The mean density of 23 g/cm^3 is compatible with the measured minimum density of the pulsar planet.²⁹

In summary, diamond, the least compressible material known, was compressed to an unprecedented density of 12 g/cm^3 , more than that of lead at ambient conditions. The measured Lagrangian sound speed, stress and density provide the first experimental data for constraining condensed-matter theory and planet-evolution models in the TPa regime. By realizing three necessary conditions, 1) the adiabatic conditions of dynamic compression; 2) a loading profile soft enough to avoid shock formation; and 3) a nearly fluid-like response of the sample such that strength and dissipation are minimal, these experiments document an approach for taking solids to the long-sought high-density conditions of statistical-electron theory.

METHODS SUMMARY

Experiments used 176 beams from the NIF laser, focused onto the inner walls of a gold hohlraum (a gold cylinder that converts the laser light to x-rays) with a combined laser energy up to 0.76 MJ in a ~ 20 -ns temporally ramped pulse. This generates a spatially uniform near blackbody distribution of thermal x-rays in the hohlraum with a characteristic radiation temperature T_r , which increases with time to a peak of $T_r \sim 235$ eV. The subsequent x-ray ablation of the diamond, over a 3-mm diameter, produces a uniform ramp-compression wave, which outruns the thermal wave produced by ablation. As the pressure wave reaches the back surface of the diamond the free surface velocity of each step is recorded with an imaging velocity interferometer (Fig. 1).

Samples consist of a 50- μm thick diamond plate used as an ablator, a 10- μm Au layer pre-heat shield, and a diamond sample having four steps (Fig. 1 inset). The diamond was synthesized by chemical vapor deposition to yield a layered microstructure with an average grain size of 200 nm and a density of 3.2491 g/cm^3 ($\pm 0.01\%$). The final sample had alternating 0.35- μm layers of 20-nm grains and ~ 350 -nm grains. X-ray diffraction showed a $\langle 110 \rangle$ texture in the growth direction. The thickness of the composite sample is determined to $\pm 1.0 \mu\text{m}$, and the differences in step thickness are determined by optical interferometry to $\pm 0.1 \mu\text{m}$. The Au layer was incorporated into the target design to serve as a radiation preheat shield for the step diamond sample. Detailed radiation transport simulations estimate a temperature rise of 33 K due to x-ray preheat.

1. Schneider, J., Dedieu, C., Le Sidaner, P., Savalle, R. & Zolotukhin, I. Defining and cataloging exoplanets: the exoplanet.eu database. *Astron. Astrophys.* **532**, A79 (2011).
2. Seager, S., Kuchner, M., Hier-Majumder, C. A. & Militzer, B. Mass-Radius relationships for solid Exoplanets. *Astrophys. J.* **669**, 1279-1297 (2007).
3. Edwards, M. J. *et al.* Progress towards ignition on the National Ignition Facility. *Phys. Plasmas* **20**, 70501 (2013).
4. Thomas, L. H. The calculation of atomic fields. *Math. Proc. Cambridge Phil. Soc.* **23**, 542-548 (1927).
5. Dirac, P. A. M. Note on exchange phenomena in the Thomas atom. *Math. Proc. Cambridge Phil. Soc.* **26**, 376-385 (1930).
6. Feynman, R. P., Metropolis N. & Teller, E. Equation of state of elements based on the generalized Fermi-Thomas theory. *Phys. Rev.* **75**, 1561-1573 (1949).
7. Salpeter E. E. & Zapolsky, H. S. Theoretical high pressure equations of state, including correlation energy. *Phys. Rev.* **158**, 876-886 (1967).
8. Abrahams A. M. & Shapiro, S. L. Cold equation of state from Thomas-Fermi-Dirac-Weizsacker theory. *Phys. Rev. A* **42**, 2530-2538 (1990).
9. Lai, D., Abrahams, A. M. & Shapiro, S. L. Equation of state in metals and cold stars: Evaluation of statistical models. *Astrophys. J.* **377**, 612-628 (1991).
10. Correa, A. A., Benedict, L. X., Young, D. A., Schwegler, E. & Bonev, S. A. A first principles multi-phase equation of state of carbon under extreme conditions. *Phys. Rev B* **78**, 024101 (2008).
11. Neaton, J.B., Ashcroft, N.W. Pairing in dense lithium. *Nature* **400**, 141-144 (1999).
12. Martinez-Canales, M., Pickard, C. J. & Needs, R. J. Theormodynamically stable phase of carbon at multiterapascal pressures. *Phys. Rev. Lett.* **108**, 045704 (2012).
13. Swift, D. C. *et al.* Mass-radius relationships for exoplanets. *Astrophys. J.* **744**, 59-68 (2012).
14. Dubrovinsky, L., Dubrovinskaia, N., Prakapenka, V. B. & Abakumov, A. M. Implementation of micro-ball nanodiamond anvils for high-pressure studies above 6 Mbar. *Nature Comm.* **3**, 1163 (2012).
15. Zel'dovich, Ya. B. & Raizer, Yu. P. *Physics of Shock Waves and High-Temperature Hydrodynamic Phenomena*, Dover (2002).
16. Atzeni S. & Meyer-ter-Vehn, J. *The Physics of Inertial Fusion: Beam Plasma Interaction, Hydrodynamics, Hot Dense Matter*, Oxford University Press, (2004).
17. Rothman, S. D. *et al.* Measurement of the principle isentropes of lead and lead-antimony alloy to ~400 kbar by quasi-isentropic compression. *J. Phys. D*, **38**, 733-740 (2005).
18. McWilliams, R. S. *et al.*, Strength effects in diamond under shock compression from 0.1 to 1 TPa. *Phys. Rev. B* **81**, 014111 (2010).
19. Vinet, P., Ferrante, J., Rose, J. H. & Smith J. R. Compressibility of solids. *J. Geophys. Res.* **92**, 9319 (1987).
20. Birch, F. Finite elastic strain of cubic crystals. *Phys. Rev.* **71**, 809 (1947).
21. Dewaele, A., Datchi, F., Loubeyre, P. & Mezouar, M. High pressure-high temperature equation of state of neon and diamond. *Phys. Rev. B* **77**, 094106 (2008).

22. Occelli, F., Loubeyre, P. & Letoullec, R. Properties of diamond under hydrostatic pressures up to 140 GPa. *Nature Mater.* **2**, 151 (2003).
23. Smith, R. F. *et al.*, Time-dependence of the alpha to epsilon phase transformation in iron. *J. Appl. Phys.* **114**, 223507 (2013).
24. Coppari, F. *et al.*, Experimental evidence for a phase transition in magnesium oxide at exoplanet pressures. *Nat. Geosci.* **6**, 926-929 (2013).
25. Sun, J., Klug, D. D. & Martoňák, R. Structural transformations in carbon under extreme pressure: Beyond diamond. *J. Chem. Phys.* **130**, 194512 (2009).
26. Eggert, J. H. *et al.*, Melting temperature of diamond at ultrahigh pressure. *Nat. Phys.* **6**, 40-43 (2009).
27. Madhusudhan, N., Lee, K. K. M. & Mousis O. A possible carbon-rich interior in super-Earth 55 Cancri e, *Astrophys. J. Lett.* **759**, L40 (2012).
28. Nettelmann, N. *et al.* Ab initio equation of state data for hydrogen, helium, and water and the internal structure of Jupiter. *Astrophys. J.* **683**, 1217–1228, (2008).
29. Bailes, M. *et al.* Transformation of a star into a planet in the millisecond Pulsar binary. *Science* **333**, 1717-1720 (2011).
30. F. W. Wagner, F. Sohl, H. Hussmann, M. Grott, and H. Rauer, Interior structure models of solid exoplanets using material laws in the infinite pressure limit. *Icarus* **214**, 366-376 (2011).

Acknowledgments: We thank the NIF staff, the Science Use of NIF program, Christoph Wild (Fraunhofer Institute for Applied Solid-State Physics, Freiburg, Germany) for preparation of the diamond targets, and Marius Millot for reanalyzing published diamond Hugoniot data. This work was performed under the auspices of the U.S. Department of Energy by Lawrence Livermore National Laboratory under Contract No. DE-AC52-07NA27344, with additional support from the Department of Energy, the University of California, and the Miller Institute for Basic Research in Science.

Author Contributions: RFS, JHE, DGB, PMC, JRP, AEL, GWC designed, executed and analyzed the data from the ramp compression experiments. JHE, RER, LXB, RJ, TSD, JW, GWC performed the comparisons of experimental data to EOS models and theory. JB, TB, AVH were instrumental in procuring and metrologizing the diamond step samples.

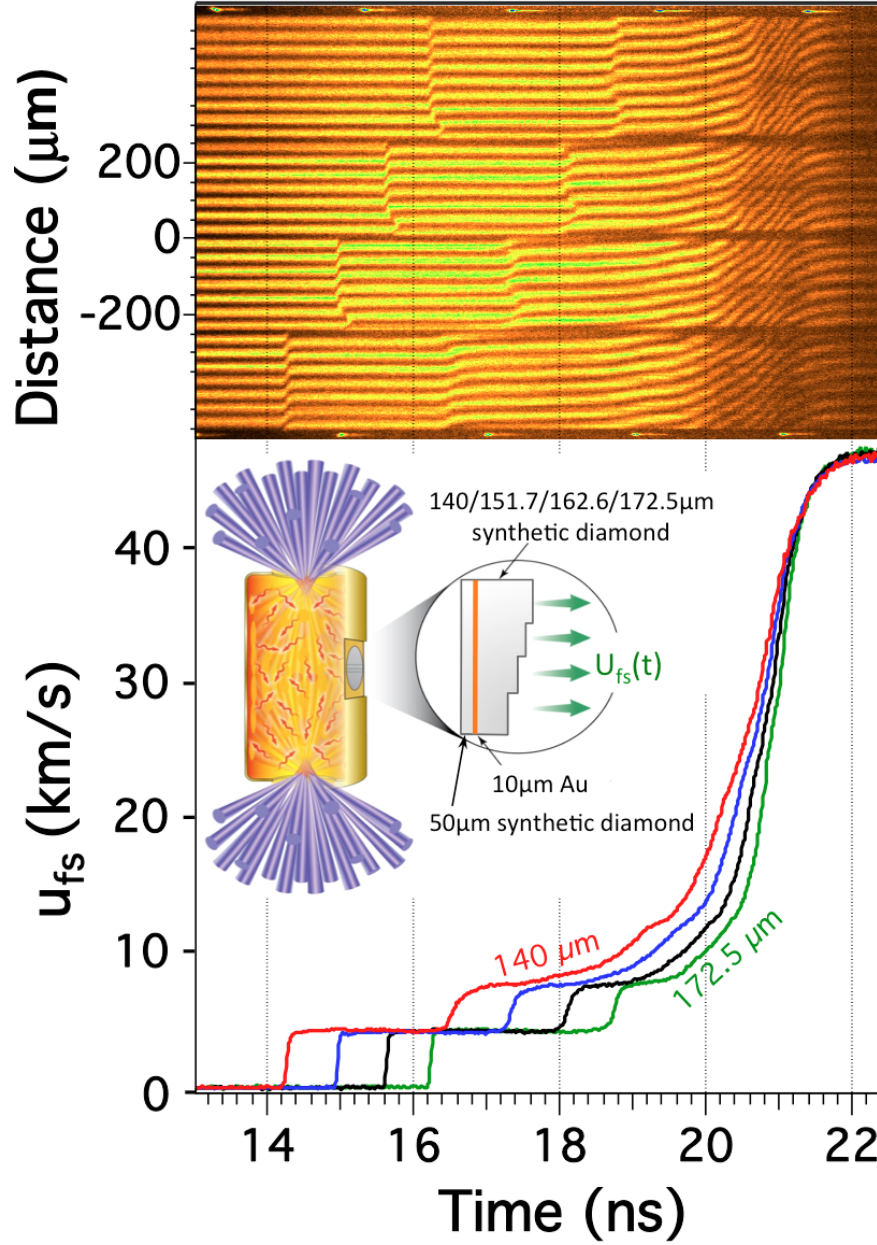


Figure 1. Velocity interferometry for ramp compressed diamond. Top image shows temporally resolved velocity interferometry record. Bottom image shows derived free-surface velocity, u_{fs} , versus time. The target (*inset*) consists of a 6-mm diameter by 11-mm long Au cylinder (hohlraum), inside of which the 351-nm wavelength laser light (*purple beams*) is converted to x-ray energy that is absorbed by the diamond sample attached to the side of the hohlraum. The x-rays ablate and ramp-compress the sample, and the free-surface velocity is recorded for four thicknesses of diamond: 140.0 μm (*red*), 151.7 μm (*blue*), 162.6 μm (*black*) and 172.5 μm (*green*) (see Methods section).

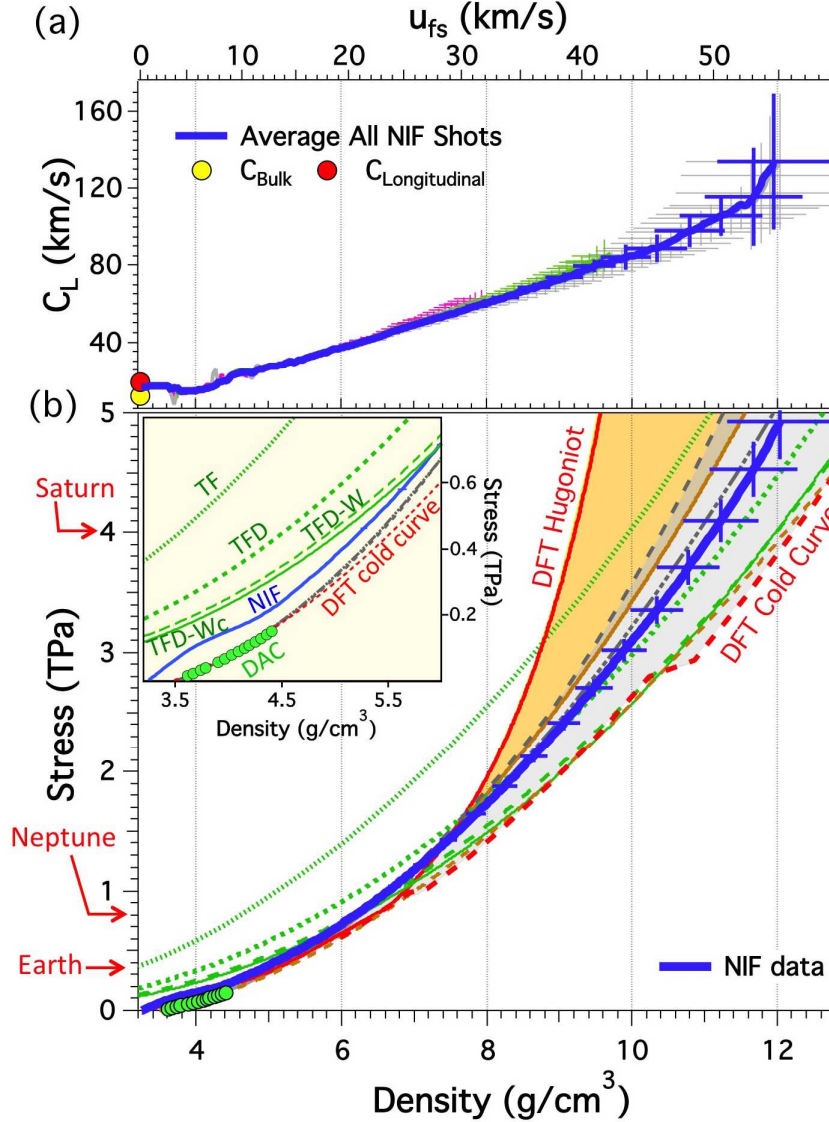


Figure 2. Ramp compression stress and sound velocity measurements. (a) Lagrangian sound velocity C_L and (b) longitudinal stress, P_x , versus density. Three experiments (*pink*, *light-green*, and *grey*) yield C_L data and their average (*dark blue*) with error bars (1σ), which, are used to determine P_x -density¹⁷ (*dark blue* in (b)). Model comparisons include: i) DFT (*solid red*)¹⁰ and Mie-Grüneisen (*solid orange*) Hugoniot (density correction discussed in Methods); ii) cold curves from DFT¹² (*red dashed*), Statistical-atom models (TF, TFD, TFD-W, and TFD-Wc as *green dotted*, *short dashed*, *long dashed* and *solid curves*)⁹, and Vinet¹⁹ (*grey dot-dash*) and Birch-Murnaghan²⁰ (*grey dash*) EOS fits to static data^{21,22}. Pressure-scale-corrected²¹ static data²² are green circles. Shaded regions between cold curves (*grey*) or Hugoniot (*orange*) show roughly the range of uncertainty in the EOS in this TPa regime. Central pressures for Earth, Neptune and Saturn are shown for reference.

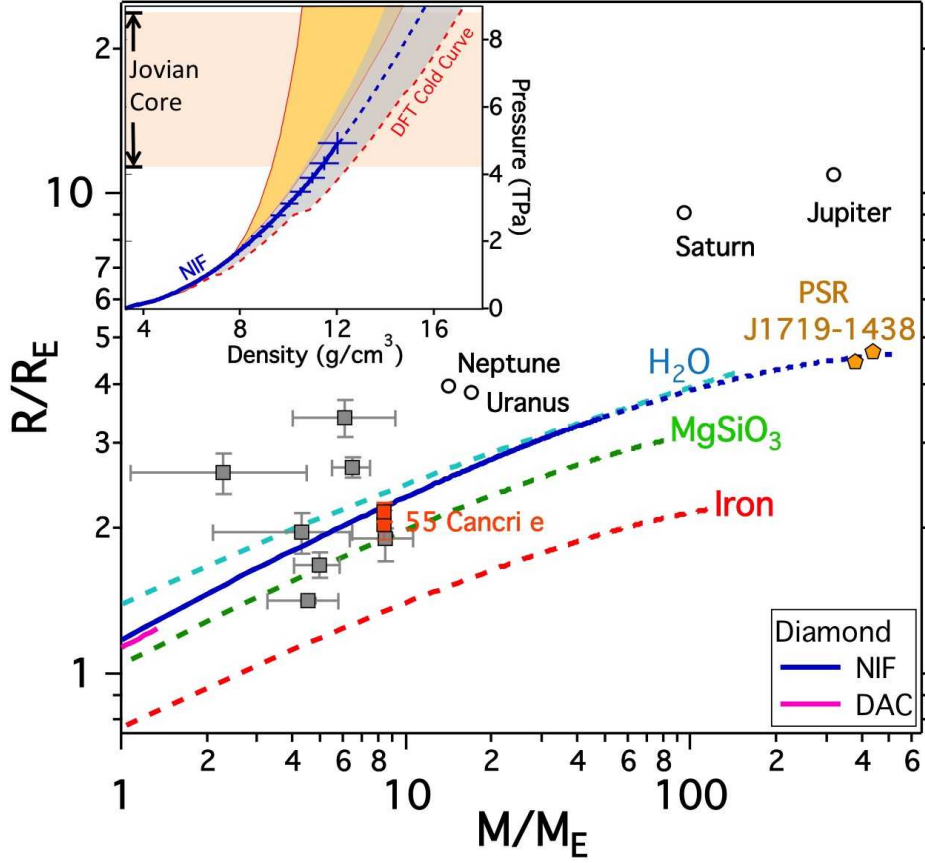


Figure 3. Mass-radius relationships for homogenous-composition planets. Calculations for carbon (based on our data where 1σ error bars are within width of line, *dark blue*), H_2O (*light blue*), post-perovskite $MgSiO_3$ (*green*) and iron (*red*)^{13,30} (curves are dashed when based on extrapolated EOS data). Yellow symbols are values consistent with the minimum density for the companion object to pulsar PSR J1719-1438 for assumed orbital inclinations of 90 and 60 degrees²⁹. The grey squares are for selected transiting super Earths. Two possible values of radii are shown for 55 Cancri e (*red squares*)²⁷. Inset shows P_x -density relevant to Jupiter's core (~ 4.3 -8.8 TPa)²⁸ with other curves as in Fig. 2.

METHODS

Ramp-compression design to TPa pressures. The inner wall of a gold hohlraum (a gold cylinder used to convert laser light to x-rays) was illuminated with 176 beams of the National Ignition Facility with a combined energy up to 0.76 MJ in a ~20 ns temporally ramped pulse. This generates a near-blackbody distribution of thermal x-rays with a characteristic radiation temperature T_r , which increases with time to a peak of $T_r \sim 235$ eV. The hohlraum was filled with 0.1 atm. of neopentayne (C_5H_{12}) gas, which enabled the hohlraum cavity to stay open so that input laser power could be coupled effectively at late times. The C_5H_{12} gas was held within the hohlraum by 0.6- μm thick polyimide windows covering the laser entrance holes. The x-ray ablation of diamond produces a uniform ramp-compression wave that transits the diamond sample. As the compression wave reaches the back of the sample, the surface accelerates into free space, and the free-surface velocity history, u_{fs} , for each step is recorded with a line-imaging velocity interferometer (VISAR) (Fig. 1). Our laser pulse shape is designed to launch an initial elastic shock into the diamond sample in advance of the ramp-compression wave. This shock feature - observed in the free-surface velocity record at $u_{fs} = 4.1$ km/s (Fig. 1) and corresponding to $P_{x,limit} = 0.11$ TPa - is interpreted as the dynamic strength (elastic limit) of diamond. The corresponding dynamic yield strength (Y_0) is determined from $Y_0 = P_{x,limit} (1 - 2\nu)/(1 - \nu)$, with the Poisson's ratio, $\nu = 0.18$, derived from our sound-speed data (Fig. 2a) from $(C_{longitudinal}/C_{bulk})^2 = 3(1 - \nu)/(1 + \nu) \left(\frac{C_{Longitudinal}}{C_{Bulk}} \right)^2 = 3 \left(\frac{1 - \nu}{1 + \nu} \right)$. This yields $Y_0 = 0.085$ TPa, which is less than observed in static experiments³¹ ($Y_0 = 0.13$ – 0.15 TPa) but consistent with the values $0.069 < Y_0$ (TPa) < 0.096 reported for ramp compression of diamond with micron grain size³². The presence of an initial shock results in a loss of diamond strength¹⁸, with expected lower levels of compressive work heating over pure ramp compression³² and, therefore, a lower temperature compression path.

Target design. Our samples consist of a 50- μm thick diamond plate used as an ablator, a 10- μm Au layer pre-heat shield, and a diamond plate having four steps (Fig. 1 inset). The diamond was synthesized by chemical vapor deposition to yield a layered microstructure with an average grain size of 200 nm and a density of 3.2491 g/cm³ ($\pm 0.01\%$).^{33,34} The final sample had alternating 0.35- μm layers of 20-nm grains and ~350-nm grains. X-ray diffraction showed a $\langle 110 \rangle$ texture in the growth direction. The thickness of the sample is determined to ± 1.0 μm , including uncertainties in the diamond ablator and Au thicknesses, whereas the differences in step thickness are determined by optical interferometry to ± 0.1 μm . The diamond sample was then attached to the Au with a ~3- μm thick glue layer. The Au layer was incorporated into the target design to serve as a radiation preheat shield. Detailed radiation transport simulations estimate a temperature rise of 33 K due to x-ray preheat.

Velocity Interferometry. Response of the sample is characterized by velocity interferometry (VISAR), which records the velocity of the sample's free (back) surface as it is engulfed by the pressure wave (Fig. 1). The VISAR (Velocity Interferometer System for Any Reflector) diagnostic uses a line-focused 660 nm-wavelength laser beam to monitor a ~1 mm strip across all four steps of the sample³⁵. Changes in velocity of the diamond free surface produce phase shifts in interference fringes that are recorded with a streak camera (Fig. 1). A typical VISAR record has a 5- μm spatial

resolution, a 10-ns streak window with 0.01 ns resolution, and a velocity resolution of 0.1 km/s.

Stress-Density analysis. Iterative Lagrangian analysis is used to translate these velocity data into a stress-density relation that quantifies the loading path (Fig. 2)^{17,36}. The Lagrangian analysis method developed by Aidun and Gupta³⁶ and modified by Rothman¹⁷ was used to determine the Lagrangian sound speed $C_L(u)$ and the stress-density ($P_x - \rho$) from the measured $u_{fs}(t)$ data, where u is the particle speed, and u_{fs} is the sample's free surface velocity (across each of four thicknesses). Metrology of the sample surface showed that the roughness was $< 0.1 \mu\text{m}$, thickness gradients were $< 1\%$, and step heights were accurate to within $0.1 \mu\text{m}$. In all, three shots gave $C_L(u)$ and $P_x - \rho$ data. $C_L(u)$ and its uncertainty $\sigma_{C_L}(u)$ are obtained from thickness and velocity vs. time data by linear regression using errors determined by our measurement accuracies: u_{fs} (0.05 km/s), time (10 ps), and step height (100 nm). The uncertainty is propagated by calculating the weighted mean average of all three shots, $\langle C_L(u) \rangle = \sum_j \frac{C_{L,j}}{\sigma_{C_L,j}^2} / \sum_j \frac{1}{\sigma_{C_L,j}^2} \Big|_u$ as

shown by the blue curve in Fig. 2a, where j is the shot number. The uncertainty in the average value is chosen from the maximum of the uncertainty in the mean and the weighted standard deviation. $\langle C_L(u) \rangle$ and $\sigma_{\langle C_L \rangle}$ are integrated to obtain

$P_x = \rho_0 \int_0^u \langle C_L \rangle du$, $\rho = \rho_0 \left(1 - \int_0^u \frac{du}{\langle C_L \rangle} \right)^{-1}$, and their uncertainties $\sigma_{P_x} = \rho_0 \int_0^u \sigma_{\langle C_L \rangle} du$ and $\sigma_\rho = \frac{\rho^2}{\rho_0} \int_0^u \frac{\sigma_{\langle C_L \rangle} du}{\langle C_L \rangle^2}$. Uncertainties are propagated through the integrals linearly, rather than in quadrature because $\sigma_{\langle C_L \rangle}$ appears to be strongly correlated rather than random. This method of uncertainty propagation allows the direct propagation of experimental uncertainties to $P_x - \rho$. Sound speed analysis over the three steps (4 thicknesses) show simple wave behavior suggesting that the material response is not time-dependent within the experimental uncertainties.

Release waves from the diamond-vacuum interface significantly perturb the incoming ramp wave. Extensive tests using simulated data confirm that the iterative Lagrangian analysis accurately corrects for these wave interactions.

Mie-Grüneisen Hugoniot and cold curve. We compare our stress-density data (Fig. 2b and Extended Data Fig. 1) to a Hugoniot and cold curve reduced from available diamond Hugoniot data. There are several ways to construct a Mie-Grüneisen equation of state, and here we begin with the relation for the pressure relative to a reference pressure P_{ref} ,

$$P(\eta, E) = P_{\text{ref}}(\eta) + \rho_0 \eta \gamma (E - E_{\text{ref}}(\eta)), \quad (1)$$

where $\eta = \frac{\rho}{\rho_0}$ is the compression, γ is the Grüneisen parameter which is assumed to depend only on density, and ρ_0 is the initial density. We can use either the Hugoniot or isotherm data to determine the reference states. Here we use the diamond Hugoniot data as the reference using a linear fit to existing shock velocity versus particle velocity data^{18,37-41},

$$Us = C + sUp \quad (2)$$

where, $C=12.0$ km/s, and $s=1.04$. From this we obtain

$$P_{ref}(\eta) = P_H(\eta) = \rho_0 \eta \frac{C^2(\eta-1)}{(\eta-s(\eta-1))^2}, \quad (3)$$

$$E_{ref}(\eta) = E_H(\eta) = \frac{C^2(\eta-1)^2}{2(\eta-s(\eta-1))^2}, \quad (4)$$

where $P_H(\eta)$ and $E_H(\eta)$ are the Hugoniot pressure and energy, respectively. Finally from Eq. 1 we obtain the cold curve

$$P_0(\eta) = \rho_0 \eta \left(\frac{C^2(\eta-1)}{(\eta-s(\eta-1))^2} + \gamma \left(E_0 - \frac{C^2(\eta-1)^2}{2(\eta-s(\eta-1))^2} \right) \right), \quad (5)$$

where we solve for $E_0(\eta)$ by,

$$\frac{dE_0}{d\eta} = \frac{1}{\rho_0 \eta^2} (P_H + \rho_0 \gamma \eta (E_0 - E_H)) = \frac{1}{\eta} \left(\frac{C^2(\eta-1)}{(\eta-s(\eta-1))^2} + \gamma \left(E_0 - \frac{C^2(\eta-1)^2}{2(\eta-s(\eta-1))^2} \right) \right). \quad (6)$$

It is also assumed $\gamma = \gamma_0 \eta^{-q}$, where $\gamma_0 = 0.85$.²¹ The variable q , has not been measured at high pressure, and can have a significant impact on the determined cold curve. We find that a value of $q = 1$ yields a cold curve centered on the DFT-calculated cold curve¹². This value of q is consistent with static measurements at pressures < 0.1 TPa.²¹ This simple model for calculating the cold curve does not incorporate volume changes from proposed high-pressure phase transformations.

Calculation of 7.6% porous Hugoniot as shown in Fig. 2 (main paper) and Extended data Fig. 1. Our samples had a measured ambient density of 3.249 g/cm³ which is 7.6% below full crystal density. To calculate the stress-density path of a 7.6% porous Hugoniot we use the expression of McQueen⁴²,

$$P_x^*(\rho) = P_H \frac{1-(\gamma/2)(\frac{\rho}{\rho_0}-1)}{1-(\gamma/2)(\frac{\rho}{\rho_0^*}-1)} \quad (7)$$

where $P_x^*(\rho)$ is the stress state along the porous Hugoniot at a density ρ , ρ_0 is the initial full crystal density (3.515 g/cc), ρ_0^* is the initial porous density (3.249 g/cc) and $\gamma(\rho)$ is the Grüneisen parameter. We note that implicit within the porous Hugoniot expression in (7) is that the wave is steady and the pores have collapsed completely in the post-shock state, i.e. $P_x^*(\rho) = 0$ for $\rho_0^* \rightarrow \rho_0$; an assumption which is incorrect for diamond. Equation (7) is therefore a poor estimate for weak shocks but in cases where the shock pressure greatly exceeds the material strength (after the pores have closed) it is reasonable.

Upon compression the material strength determines how much stress is needed to reduce the porosity to a given level. This relationship can be summarized in a crush-up curve: $\rho = \rho(\rho_0^*, P_x^*, E)$.⁴³⁻⁴⁵ Following Carroll and Holt⁴⁴, pore crush-up is only initiated after a critical longitudinal stress, $P_{crit} = \frac{2}{3} Y_0 |\ln f_0|$ where Y_0 is the yield strength and f_0 is the initial porosity. For our diamond samples $Y_0 = 0.085$ TPa, $f_0 = \rho_0^*/\rho_0 = 0.076$ and $P_{crit} = 0.146$ TPa. For $0 \leq P \leq P_{crit}$, the pressure-dependent pore fraction $f = f_0$ and the material is assumed to deform elastically. For $P > P_{crit}$, the porosity decays exponentially as $f = e^{-3P_x/2Y_0}$.

A number of studies on shock compression of under-dense materials have shown that rapid heating due to pore closure and the resultant increase in thermal pressure gives rise to reduced compression.⁴² In Extended Data Fig. 1 this is witnessed by the stiffer response of the calculated porous Hugoniot compared to the Hugoniot for full-density diamond.

Summary of Diamond EOS data and DFT calculations. Extended Data Figure 1 compares our data (initial density $\rho_0 \sim 3.249 \text{ g/cm}^3$) with previously reported shock Hugoniot,^{18, 37-41} static,²² and ramp compression³² data ($\rho_0 \sim 3.515 \text{ g/cm}^3$) as stress vs. density. Shock Hugoniot data rely on knowledge of a reference material and therefore subsequent revisions of the reference EOS can change the reported diamond Hugoniot data. The Hugoniot points shown in Extended Data Fig. 1 have been reanalyzed to account for new standard EOS as follows: The data reported by Nagao³⁸ and Bradley³⁹ have been reanalyzed using an aluminum standard impedance matching⁴⁶ with the latest fit to the Al Hugoniot⁴⁷. The highest pressure point of Bradley used a Mo standard and remains unchanged. The data reported by Hicks⁴¹ and Brygoo⁴⁰ used a quartz standard. These data have been reanalyzed using the constant Grüneisen re-shock model in Ref. 41 and the quartz Hugoniot used as a reference is a fit of all available data for alpha-quartz shocked into the liquid phase.^{47,48}

The DFT EOS we use to produce the Hugoniot in Fig. 2 and Extended Data Fig. 1 is as reported in Ref. 10, except without the embedding into the Thomas-Fermi-based QEOS model. We omit the connection with the QEOS model because the transition region between *ab-initio* and QEOS models in Ref. 10 created unphysical kinks in the EOS and resulting Hugoniot. The extrapolation of the more limited-range *ab-initio* EOS of Ref. 10 to the conditions relevant for the Hugoniot final states shown in our figures is expected to be quite accurate⁴⁹. The DFT cold curve generated from Ref. 10 is in good agreement with the DFT cold curve reported in Ref. 12 (red dashed curve in Figs. 2 and Extended Data Fig. 1) for stresses less than 2.5 TPa (which is the pressure below which *ab initio* electronic structure information was used to construct that EOS).

Static-compression and elasticity measurements to 0.15 TPa are indistinguishable from the cold curves presented here^{21,22}. The fit to the static compression measurements over this low compression range ($\rho/\rho_0 \ll 1$) are insensitive to the form of EOS used to fit the data (e.g., Vinet¹⁹, Birch-Murnaghan²⁰, or Holzapfel⁵⁰). The Vinet EOS plotted in Fig. 2 and Extended Data Fig. 1 use $K_0 = 445 \text{ GPa}$ and $K'_0 = 4.18$ as reported in Ref. 21. The values used for the Birch-Murnaghan ($K_0 = 445 \text{ GPa}$, $K'_0 = 3.90(0.04)$) and Holzapfel ($K_0 = 445 \text{ GPa}$, $K'_0 = 3.95(0.05)$) forms of EOS are based on fits to previous isothermal data.^{21,22} Here the values from Ref. 22 have been reanalyzed using the revised ruby pressure scale as reported in Ref. 21. Extrapolating these isothermal data to the multi-TPa regime becomes highly uncertain depending on the EOS used (Fig. 2b and Extended Data Fig. 1).

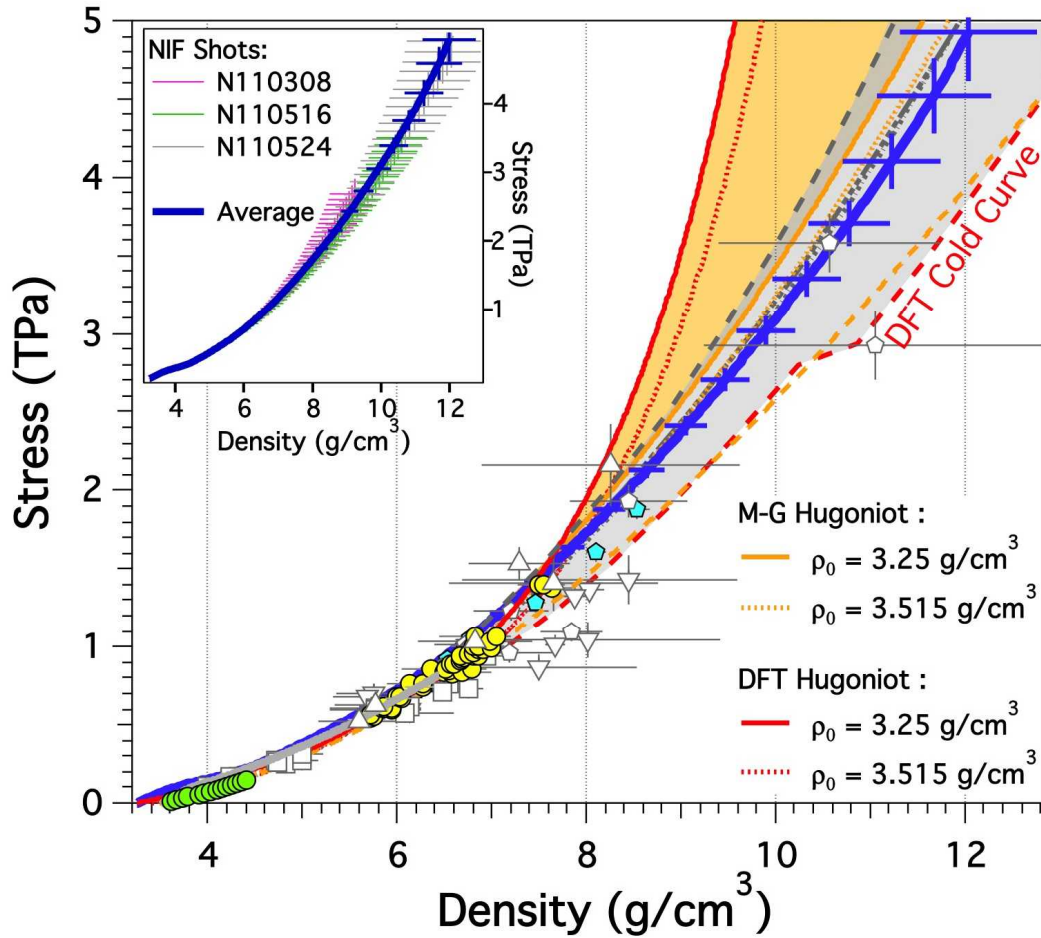
31. Eremets, M. I. *et al.* The strength of diamond. *Appl. Phys. Lett.* **87**, 141902 (2005).

32. Bradley, D. K. *et al.* Diamond at 800 GPa. *Phys. Rev. Lett.* **102**, 075503 (2009).

33. Reichart, P. *et al.* Three-dimensional hydrogen microscopy in diamond. *Science* **306**, 1537 (2004).

34. Dawedeit, C. *et al.* Grain size dependent physical and chemical properties of thick CVD diamond films for high energy density physics experiments, *Diamond and Related Material* **40**, 75-81 (2013).
35. Celliers P. M. *et al.* Line-imaging velocimeter for shock diagnostics at the Omega laser facility. *Rev. Sci. Instrum.* **75**, 4916 (2004).
36. Aidun J. B. & Gupta Y. M. Analysis of Lagrangian gauge measurements of simple and nonsimple plane waves. *J. Appl. Phys.* **69**, 6998 (1991).
37. Knudson, M. D., Desjarlais, M. P. & Dolan, D. H. Shock-wave exploration of the high-pressure phases of carbon. *Science* **322**, 1822 (2008).
38. Nagao, H. *et al.* Hugoniot measurement of diamond under laser shock compression up to 2 TPa. *Phys. Plas.* **13**, 052705 (2006).
39. Bradley shock data reported in ref [41].
40. Brygoo, S. *et al.* Laser-shock compression of diamond and evidence of a negative-slope melting curve. *Nat. Mat.* **6**, 274 (2007).
41. Hicks, D. G. *et al.*, High-precision measurements of the diamond Hugoniot in and above the melt region. *Phys. Rev. B* **78**, 174102 (2008).
42. McQueen, R. G., Marsh, S. P., Taylor, J. W., Fritz, J. N. & Carter, W. J. The equation of state of solids from shock wave studies. in *High Velocity Impact Phenomena* (Academic Press, New York, 1970) Ch. 7, pp. 293–417.
43. Herrmann, W. Constitutive Equation for the Dynamic Compaction of Ductile Porous Materials. *J. Appl. Phys.* **40**, 2490 (1969).
44. Carroll, M. M. & Holt, A. C. Static and Dynamic Pore Collapse Relations for Ductile Porous Materials. *J. Appl. Phys.* **43**, 1626 (1972).
45. Reisman, D. B., Wolfer, W. G., Elsholz, A. & Furnish, M. D. Isentropic compression of irradiated stainless steel on the Z accelerator. *J. Appl. Phys.* **93**, 8952 (2003).
46. Celliers, P. M., *et al.* Systematic uncertainties in shock-wave impedance-match analysis and the high-pressure equation of state of Al. *J. Appl. Phys.* **98**, 113529 (2005).
47. Knudson, M. D. & Desjarlais, M. P. Adiabatic release measurements in α -quartz between 300 and 1200 GPa: Characterization of α -quartz as a shock standard in the multimegabar regime. *Phys. Rev. B* **88**, 184107 (2013).
48. Hicks, D.G. *et al.*, Shock compression of quartz in the high-pressure fluid regime. *Phys. Plasma* **12**, 082702 (2005).
49. Benedict, L. X. *et al.* A multiphase equation of state for carbon addressing high pressures and temperatures. *arXiv preprint arXiv:1311.4577* (2013).
50. Holzappel, W. Equations of state for ideal and real solids under strong compression. *Europhys. Lett.* **16**, 67 (1991).

Extended Data



Extended Data Figure 1. Ramp compressed diamond stress versus density compared to other high-pressure data. NIF ramp-compression data with 1-sigma error bars (*solid blue*) together with calculated Hugoniots (low initial density diamond, *solid red*; standard initial density diamond, *dotted red*) and the calculated cold curve (*dashed red*)¹² from DFT; a simple Mie-Grüneisen model reduction of Hugoniot data to produce an extrapolated Hugoniot (low initial density diamond, *solid orange*; standard initial density diamond, *dotted orange*), and cold curve (*dashed orange*); Vinet¹⁹ (*dot-dashed grey*), Birch-Murnaghan²⁰ (*dashed grey*), and Holzappel⁵⁰ (*dotted*) extrapolations of 300 K DAC data.^{21,22} The shaded regions show the range of different models for cold curve (*grey*) and Hugoniot (*orange*) showing roughly the range of uncertainty in this ultra-high pressure regime. Also shown are data from shock experiments [Knudson³⁷ (*yellow circles*), Nagao³⁸ (*up triangle*), Bradley³⁹ (*open hexagon*), Brygoo⁴⁰ (*down triangle*), Hicks⁴¹ (*blue hexagon*), MacWilliams¹⁸ (*open squares*)], isothermal static data [*green circles* are ruby-corrected data^{21,22}] and the ramp-compression data of Bradley³² (*solid gray curve*). The ramp-compression data of Bradley used full density diamond and did not use an initial shock as in NIF data. Shown as inset are calculated stress-density relations of the three NIF shots: N110308, N110516 and N110524 showing the level of repeatability between experiments.

Extended Data Table 1: Ramp-compressed diamond stress-density data.

Stress (GPa)	Stress Uncertainty (GPa)	Density (g/cm³)	Density Uncertainty (g/ cm³)
0.0	0.0	3.25	0.00
9.7	0.1	3.29	0.00
19.5	0.2	3.32	0.00
29.4	0.3	3.36	0.00
39.2	0.3	3.40	0.00
49.2	0.4	3.44	0.00
59.1	0.5	3.48	0.00
69.0	0.6	3.53	0.00
79.0	0.7	3.57	0.00
89.0	0.8	3.61	0.00
98.8	0.8	3.66	0.00
107.8	0.9	3.71	0.00
117.0	1.0	3.76	0.01
125.4	1.1	3.82	0.01
133.8	1.1	3.88	0.01
142.4	1.2	3.94	0.01
151.0	1.3	4.00	0.01
159.7	1.3	4.07	0.01
168.7	1.4	4.13	0.01
178.0	1.5	4.19	0.01
187.8	1.6	4.25	0.01
198.5	1.7	4.31	0.01
210	1.9	4.37	0.01
221	2.0	4.42	0.01
234	2.1	4.48	0.02
247	2.3	4.53	0.02
261	2.4	4.58	0.02
275	2.6	4.63	0.02
289	2.8	4.69	0.02
304	3.0	4.74	0.02
318	3.2	4.79	0.02
333	3.4	4.85	0.02
348	3.6	4.90	0.02
363	3.8	4.95	0.03

379	4.0	5.00	0.03
396	4.3	5.06	0.03
412	4.5	5.11	0.03
428	4.7	5.17	0.03
445	5.0	5.22	0.03
462	5.2	5.27	0.03
480	5.5	5.33	0.04
498	5.8	5.38	0.04
516	6.0	5.44	0.04
534	6.3	5.49	0.04
553	6.6	5.55	0.04
572	6.9	5.60	0.04
592	7.3	5.66	0.05
612	7.6	5.71	0.05
632	7.9	5.77	0.05
653	8.3	5.82	0.05
674	8.7	5.88	0.05
695	9.1	5.93	0.05
717	9.5	5.99	0.06
739	9.9	6.05	0.06
762	10	6.10	0.06
785	11	6.16	0.06
808	11	6.21	0.07
832	12	6.27	0.07
856	12	6.32	0.07
880	13	6.38	0.07
905	13	6.44	0.07
930	14	6.49	0.08
955	14	6.55	0.08
981	15	6.61	0.08
1008	15	6.66	0.09
1035	16	6.72	0.09
1062	17	6.78	0.09
1090	17	6.83	0.09
1118	18	6.89	0.10
1147	19	6.95	0.10
1176	19	7.00	0.10
1205	20	7.06	0.11
1235	21	7.12	0.11
1265	21	7.18	0.11
1296	22	7.23	0.12

1327	23	7.29	0.12
1358	24	7.35	0.12
1390	25	7.41	0.13
1422	25	7.47	0.13
1454	26	7.52	0.13
1487	27	7.58	0.14
1521	28	7.64	0.14
1554	29	7.70	0.14
1588	30	7.76	0.15
1623	31	7.82	0.15
1658	32	7.88	0.16
1694	33	7.94	0.16
1729	34	8.00	0.16
1766	35	8.06	0.17
1802	37	8.12	0.17
1839	38	8.18	0.18
1877	39	8.24	0.18
1915	40	8.31	0.19
1953	42	8.37	0.19
1992	43	8.43	0.20
2032	44	8.49	0.20
2071	46	8.55	0.21
2112	47	8.61	0.21
2152	49	8.68	0.22
2194	50	8.74	0.22
2235	52	8.80	0.23
2277	54	8.86	0.24
2320	55	8.93	0.24
2363	57	8.99	0.25
2406	59	9.05	0.25
2450	60	9.12	0.26
2495	62	9.18	0.27
2540	64	9.25	0.27
2585	66	9.31	0.28
2632	68	9.37	0.28
2678	70	9.44	0.29
2726	72	9.50	0.30
2774	74	9.57	0.30
2822	76	9.63	0.31
2871	79	9.70	0.32
2920	82	9.76	0.33

2969	85	9.83	0.34
3019	88	9.90	0.35
3069	92	9.96	0.36
3119	96	10.03	0.37
3170	100	10.10	0.38
3222	104	10.17	0.39
3273	108	10.23	0.40
3326	112	10.30	0.41
3379	116	10.37	0.42
3432	121	10.44	0.43
3486	125	10.51	0.44
3541	130	10.58	0.45
3596	134	10.65	0.46
3653	139	10.71	0.48
3710	144	10.78	0.49
3768	149	10.85	0.50
3827	155	10.92	0.51
3887	160	10.99	0.53
3947	165	11.06	0.54
4008	171	11.13	0.55
4070	177	11.19	0.56
4133	183	11.26	0.58
4196	189	11.33	0.59
4260	195	11.40	0.61
4324	202	11.47	0.62
4390	208	11.54	0.63
4457	215	11.60	0.65
4524	228	11.67	0.67
4592	242	11.74	0.69
4663	258	11.81	0.72
4736	275	11.87	0.74
4811	293	11.94	0.76
4889	313	12.00	0.79
4929	323	12.03	0.80